Link to the publisher version: https://doi.org/10.1016/j.ijsolstr.2023.112178

A mechanical model for compaction of strands for wire ropes

Li Chen[a], Marco Magliulo[b], Marco Elig[c], Lars A.A. Beex[a*]

[a] Faculté des Sciences, de la Technologie et de la Communication, Université de Luxembourg, Maison du Nombre, Avenue de la Fonte 6, L-4364 Esch-sur-Alzette, Luxembourg

[b] Kiswire International S. A., Z.A.E. Wolser F 312, L-3290 Bettembourg, Luxembourg

[c] KV R&D Center GmbH, Seilmacherstraße 7,D-66497 Contwig, Germany

Abstract

Steel wire ropes are used for numerous industrial applications such as ships, elevators, cranes and bridges. A wire rope consists of numerous thin, steel wires and its geometrical construction can be explained in two steps. First, several wires are wrapped together in a helical shape called a strand. Second, several strands are wrapped together in a helical shape to form the final wire rope. In most cases, each strand is compacted before they are wrapped together to form the final wire rope. Compaction generally reduces contact stresses and thereby, extends ropes' service life. Not many models have been proposed to predict the compaction process and its influence on the strand's mechanical behaviour during service. This contribution proposes a computationally efficient approach that consists of two elastoplastic mechanical models. The first model, describing the compaction process, is of a 2D plane strain nature and is therefore fast. Subsequently, the 2D geometry and plastic variables predicted by the compaction model are used to generate the initial geometry and initial plastic state of a 3D model, that is subsequently used to describe the strand's mechanical behaviour during service (we limit ourselves to tension). The results of the approach, with and without the mapping of the plastic variables, are compared to experimental measurements and the results without compaction. This is investigated for two real world strands.

Keyword: rope, strand, compaction, elastoplasticity, contact.

*Corresponding author. Tel.: (+352) 46 66 44 5646; fax: N.A.. E-mail address: lars.beex@uni.lu.

1 Introduction

Thanks to their excellent load bearing capacity and flexibility, wire ropes are widely applied in hoisting and load-carrying scenarios such as suspension bridges, elevators and cranes. They are also used in scenarios where combined mechanical and electric performances are the primary concern, such as power lines [34] and superconducting cables [20]. A strand is manufactured by twisting thin wires with circular cross sections around a straight wire. Simply speaking, the final wire rope is formed by twisting the strands around a straight strand/rope. In Fig. 1, a more complex design is depicted however, as the central straight strand is in fact not a strand, but a small wire rope.

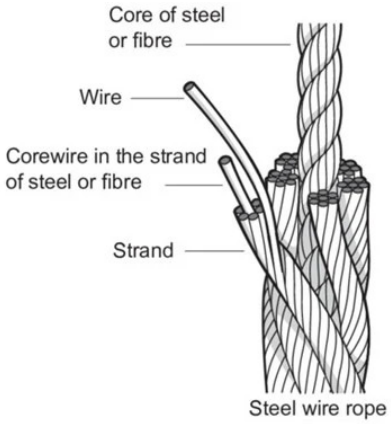

Figure 1: Composition of a wire rope [2].

Many design variables affect the design of strands and wire ropes. Examples are the diameters of the thin wires, the number of wires in each strand and the number of strands in a wire rope [1,3]. Another design variables is the lay length L_{lay}, which is the distance in axial direction required to complete one revolution of a peripheral wire/strand around the central wire/strand. It may be clear that a wire rope comes with at least two lay lengths: the lay length describing the rotation of the peripheral strands around the central strand, and the lay length describing the rotation of the peripheral wires around the central wire in each strand. A wire ropes also comes with at least two lay directions (i.e. a binary variable), which quantifies whether the rotations are clock-wise or counter-clock-wise.

Mechanical predictions can help to optimize wire rope designs. Yet, the fact that many de-

formable bodies are in contact with each other within a wire rope (i.e. up to hundreds thin wires) makes the mechanics occurring during a wire rope's manufacturing and service highly complex [22]. If a wire rope will often be rolled up around a pulley during service (when used in cranes for instance) furthermore, the inter-wire contacts will experience a substantial amount of cyclic relative sliding, causing wear and fatigue failure [17, 28, 32], which is not relevant to consider for static wire ropes (e.g. those in suspension bridges).

Nowadays, the practice of compaction is widely exploited to enhance the mechanical performance of strands and wire ropes. Compaction is a procedure that forces strands/ropes to pass through a series of dies or rollers to plastically compress the strands or ropes. Compaction flattens the surface of contact between adjacent wires in a strand or adjacent strands in a rope (see Fig. 2 for a compacted strand). Thus, it increases the contact area and reduces the contact pressure and fretting wear as a result. When compaction is applied to strands, before the strands are twisted together to form the final wire rope, the obtained rope is termed a *strand compacted rope*. When compaction is applied to an entire wire rope, the resulting rope is termed a *swage compacted rope* [10].

Investigations into the mechanical improvement of the compacted strand/rope are first carried out by experiments. Danenko, et al. [5] have experimentally studied the improved mechanical performance of plastically compacted steel strand/rope compared to their uncompacted counterparts. Torgersen [27] has experimentally investigated the fatigue and wear resistance in compacted steel wire ropes, as well as the relationship between the number of visibly broken wires and the remaining strength of the rope. Szade et al. [26] have experimentally studied the thermoelastic performance of compacted steel wire ropes under uniaxial loading with the help of infrared images. What is shown in the experimental studies is that both the geometry and the compaction induced work hardening play significant roles when it comes to improving the mechanical performance. These two fators will be accounted for in the proposed numerical model of the present work.

To guide the virtual design process of wire ropes, as well as to obtain a better understanding of their mechanics, numerous analytical and numerical studies have been carried out. Costello [4] for instance performed a theoretical analysis on the mechanical aspects of wire strands/ropes based on the thin rod theory of Love [18]. Closed-form expressions for quantities of interest, such as the elastic stiffness and the inter-wire contact force, are derived for strands/ropes under tension and

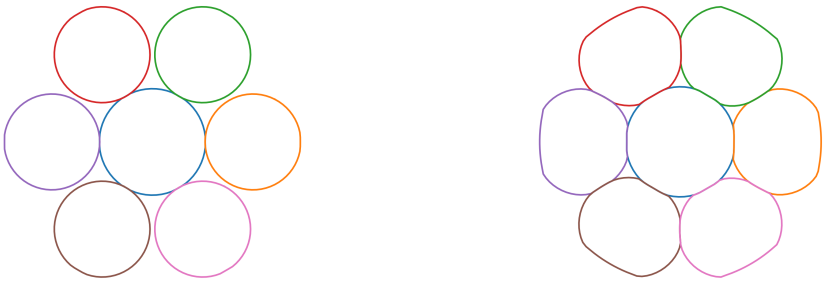

(a) Before compaction. (b) After compaction.

Figure 2: Cross-sectional sketch of a 1+6 strand before and after compaction.

bending around a sheave. However, infinitesimal elasticity is presumed and only wires with circular cross sections are considered. These analytical models are not capable of debunking more arcane phenomena such as the fretting wear depth of crossed wires.

Wu and Cao [33] presented closed-form expressions for the force–deformation relation of wire ropes after establishing the rope geometry using Frenet frame and differential geometry. In terms of the wire behavior, the elastic thin rod theory of Love [18] was adopted. Again, the research is restricted to infinitesimal elasticity and circular wire cross sections. Elata et al. [8] have proposed closed-form formulations to predict the elastic stiffness coefficients of a rope. Two configurations were considered: (1) fully lubricated rope without inter-wire friction and (2) infinite inter-wire friction that disables relative displacements. The assumptions regarding the thin rod theory, the material model and the circular wire cross section limit the application regime of these theoretical studies. The introduction of compacted wire rope, plastic injected wire rope and fibre filled wire rope further restricts the applicability of analytical models.

Numerical modeling and finite element based simulation may serve as alternatives to demystify and predict the mechanical behavior of wire rope. As reliable numerical models build on accurate geometries, creating precise geometrical computer representations for wire strands/ropes is intensively studied. Stanova et al. [23,24] and Imrak et al. [13] have for instance formulated parametrizations for the centroid lines of wires in a straight strand/rope using single and double helical equations. Single helices are used to portray either the peripheral wires in a straight strand or the central wire in a

side strand of a straight rope. Double helices are used to portray the peripheral wires of a peripheral strand in a straight rope. Wang et al. [30] further extended the aforementioned parametrization in order to portray the centroid line of a wire in an arbitrarily curved and twisted rope. Hitherto, the parameterization hinges on circular wire cross sections.

Based on this, finite element models with varying element types (i.e. beam elements/solid elements) and solution schemes (i.e. static/dynamic) are applied to study a variety of complex behaviors and properties of strands/ropes that are beyond the capacity of analytical models. For instance, de Menezes et al. [6] have applied a variety of models to predict the tensile/torsional/bending response of a single-layered strand under a wide range of helical angles and have systematically compared the models in terms of accuracy. The models have included an analytical model, a finite element model using beam elements, a finite element model using solid elements in a quasi-static setting and a finite element model using solid elements in a dynamical setting.

Jiang et al. [15] have proposed a concise finite element model for straight strands, where only a single layer of elements is used in the strand axial direction after taking full advantage of the helical periodicity of a strand. The proposed model, although only applied to a straight 1+6 strand, enables to study the contact stress, residual stress, friction and plastic deformation. The proposed model has been extended by Jiang et al. [14] to account for a three-layered straight strand, where more layers of elements have been used in the axial direction to capture the non-uniform stress distribution in the peripheral wires due to the trellis point contact. Wang et al. [29] have combined finite element analysis with Archard's wear law to predict the evolution of fretting wear depth for crossed wires as well as the implied fatigue life. The results have shown that both different wires in the rope or strand and distinct material models in the analyses induce different stress distributions and fretting fatigue parameters. The predicted fretting wear depths of wires show good agreement with experimental results.

However, it is worth noting that a majority of the numerical researches only consider circular wires. In other words, the literature predominently focuses on modeling of *uncompacted* strands/ropes, whereas hardly any research has focused on *compacted* strands/ropes.

To the best of the authors' knowledge, only a handful of works have focused on the mechanical modeling of compacted strands/ropes. This is somewhat surprising, since these days many wire

ropes are compacted or include compacted strands. Resorting to a finite element model in Abaqus, Zeroukhi et al. [34] have modeled the compacting process of a concentric conductor $1 + 6$ strand by pulling the straight, virtual strand through a 3D compacting die. This modelling approach reveals the plastic deformation induces by the compacting process. A disadvantage of this approach is that it can only be applied to a single strand or a swage compacted wire rope. If an entire wire rope with compacted strands is to be modeled with this approach, another modeling step must be included in which the (compacted) strands are virtually wound around the central (compacted) strand. However, the most important disadvantage of this approach is its substantial computational time.

On the other hand, Erdönmez [9] presented a completely different modelling approach, which only includes the effect of compaction on subsequent simulations of the wire rope during service, e.g. during tension, bending and torsion. In the approach of Erdonmez, the compaction process itself is not predicted. Instead, the wires' cross sectional shapes resulting from real world compaction are registered using experimental photos. The plastically deformed wires' cross sectional shapes are then included in a finite element model of the wire rope during service. In this way, similarity between the real compacted strand and the finite element model is preserved in terms of geometry, but the spatially varying work hardening induced by the compaction process is not incorporated. More importantly, the approach is unable to predict the effect of the amount of compaction on the wire rope's behaviour during service. In [10], Erdönmez further combines the parametric mathematical curve equations (which are used to describe the compacted sectional shape of wires) with the parametric equations of single and double helices (which are used to portray the centroid lines of wires) so as to build the geometry and mesh for the finite element model of a multi-layered compacted wire rope. Again, compaction induced, spatially fluctuating work hardening is unavailable and can therefore not be incorporated. Moreover, the proposed modeling scheme is only feasible for compacted strand and strand compacted rope.

It is thus clear that the amount of proposed compaction models does not correspond with the current demand of compacted strands and compacted wire ropes in the industry. The present contribution proposes a new modeling scheme able to efficiently yet accurately predict the compaction process itself, as well as the effect of the compaction process in the subsequent simulations of the

strand during service. The proposed modeling scheme relies on a two-step procedure. In the first step, a 2D (and thus computationally efficient) finite element model is established for the strand cross section. The 2D cross section model simulates the compaction process so that not only the deformed shape but also the field of compaction induced plastic deformation is predicted in great detail within each wire. In the second step, a 3D finite element model is established for the strand. The 3D strand model serves to simulate the strand's mechanical behaviour during service life. Although this may include bending and torsion, we only focus on tension. From the subsequent 3D simulation results, key quantities of interest, such as elastic moduli and yield forces, can be extracted.

The 3D strand model inherits the cross sectional strand shape predicted by the 2D model. Moverover, the 2D field of equivalent plastic strains predicted by the 2D compaction model is projected onto the 3D strand model. The proposed modeling scheme is thus less computationally demanding than the modeling scheme proposed by Zeroukhi et al. [34], because our compaction model is 2D. At the same time, it is more capable than the schemes of Erdönmez [9,10] because the compaction process is truly modeled.

The presented work is organized as follows: in Section 2, the 2D strand cross section model for the purpose of compaction simulation is described in detail. In Section 3, the method to construct the 3D model of compacted strands is elaborated, with an emphasis on the transfer of the compacted strand cross sectional shape and the compaction induced plasticification predicted by the 2D model in Section 2. In Section 4, numerical simulations are performed for two benchmark strand designs. The numerical predictions in terms of the tensile response are compared to their experimental counterparts. In Section 5, conclusions on the proposed modeling scheme are presented.

In what follows, the following notation is used:

- Scalars are denoted by small case and capital letters: e.g. a and A.
- Column matrices are denoted by underlined small case letters: e.g. $\underline{a}$.
- Matrices are denoted by twice underlined capital letters: e.g. $\underline{\underline{A}}$.
- Vectors are denoted by bold small case letters: e.g. $\mathbf{a}$.
- Second order tensors are denoted by bold capital letters: e.g. $\mathbf{A}$.

- Fourth order tensors are denoted by bold capital letters and superscript 4: e.g. ${}^4\mathbf{A}$.

2 2D compaction model

This section elaborates on the establishment of 2D finite element model for the strand cross section subjected to compaction. Both the 2D compaction model and the subsequent 3D model of the next section are created using commercial finite element software Abaqus.

2.1 Geometry

As a first step, the cross sectional shape of a strand needs to be established. This is not a straightforward task because even if each wire is assumed to be circular, the peripheral wires (in contrast to the straight central wire of a strand) exhibit elliptical cross sections when viewed in the direction of the strand axis. The ellipticity depends on the lay length and the diameter of the peripheral and central wires in the strand. In the present work, a new procedure is proposed to determine the elliptical shape of the peripheral wires in the cross section in the direction of the strand's axis.

Firstly, the equations of [23] help to describe the centroid line of a helical peripheral wire in a straight strand:

$$\begin{cases} x(\phi) & = r_j \cos(\xi_{ij} + q\phi) \\ y(\phi) & = r_j \sin(\xi_{ij} + q\phi) \\ z(\phi) & = \phi \frac{r_j}{\tan(\alpha_j)} \end{cases} \tag{1}$$

where q denotes the lay direction and is $q = 1$ for a right hand lay and $q = -1$ for a left hand lay. α_j and r_j denote the lay angle and the lay radius of the peripheral wire in the j^{th} layer of the strand, respectively. ξ_{ij} denotes the phase angle between the i^{th} wire in j^{th} layer and the reference wire in the same layer. ϕ denotes the phase angle. It can be noted that the peripheral wires of different layers all have the same phase angle, but not the same lay radius. Therefore, the position vector of the centroid line of the peripheral wire can be expressed in Cartesian frame as

$$\mathbf{r} = x(\phi)\mathbf{i} + y(\phi)\mathbf{j} + z(\phi)\mathbf{k}, \tag{2}$$

where **i**, **j** and **k** denote basis vectors. Note that the lay angle refers to the angle between the tangent of the helical peripheral wire and the plane perpendicular to the strand axis. The lay length can be obtained as $L_{lay} = 2\pi r_j \tan(\alpha_j)$.

Secondly, the Frenet–Serret formulas [31] are used to portray the helix. Particularly, the tangent, normal, and binormal unit vectors (denoted by **t**, **n**, **b**, respectively), or collectively referred to as the Frenet–Serret frame or TNB frame, together form an orthonormal basis spanning $\mathbf{R}^3$ and can be computed for each point on the curve. The definitions of aforementioned unit vectors are:

- **t** denotes the unit vector tangent to the centroid: $\mathbf{t} = \frac{\mathrm{d}\mathbf{r}}{\mathrm{d}\phi} / ||\frac{\mathrm{d}\mathbf{r}}{\mathrm{d}\phi}||$;
- **n** denotes the normal unit vector, and is the derivative from **t** with respect to the arclength parameter of the centroid, divided by its length, i.e. $\mathbf{n} = \frac{\mathrm{d}\mathbf{t}}{\mathrm{d}\phi} / ||\frac{\mathrm{d}\mathbf{t}}{\mathrm{d}\phi}||$;
- **b** denotes the binormal unit vector, the cross product of **t** and **n**, i.e. $\mathbf{b} = \mathbf{t} \times \mathbf{b}$.

For comprehension, the Frenet–Serret frame for a helix is graphically illustrated in Fig. 3.

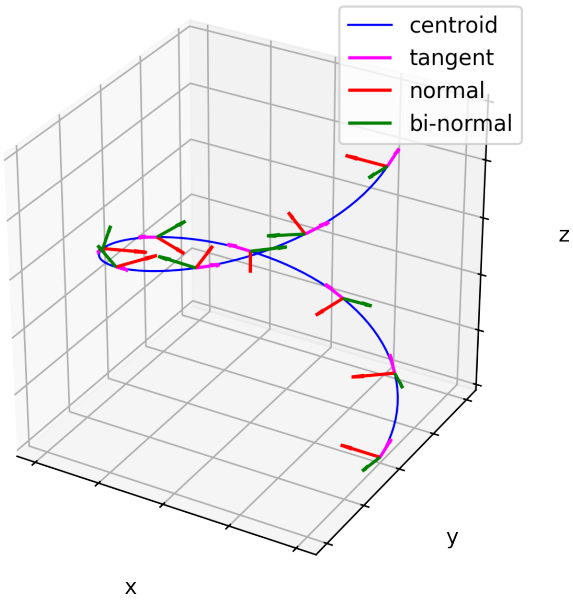

Figure 3: TNB frame for a helix.

Thirdly, the elliptical profile of a peripheral wire viewed in the direction of the strand axis is computed. This constitutes the computation of the intersection of a peripheral wire with a cutting

plane that is parametrized by $z = z_0$ (where the axis of the strand coincides with the z-axis in Eq. (1)).

As is shown in Fig. 4, the position vector of the centroid is denoted by $\mathbf{r}$, which is established using Eq. (1). Meanwhile, the Frenet–Serret frame is established for the cross section so that the three unit vectors, $\mathbf{t}$, $\mathbf{n}$ and $\mathbf{b}$, are obtained. With the help of the TNB frame, the position vector of an arbitrary point on the circumference of a wire's cross section can be formulated as:

$$\bar{\mathbf{r}}(\phi,\theta) = \mathbf{r}(\phi,\theta) + R_{\mathrm{w}}\cos(\theta)\mathbf{n}(\phi) + R_{\mathrm{w}}\sin(\theta)\mathbf{b}(\phi) \tag{3}$$

where R_{w} denotes the radius of the wire. θ denotes an azimuthal angle defined in the wire's cross section, where $\mathbf{n}$ and $\mathbf{b}$ serve as basis vectors. By solving $\bar{\mathbf{r}}_z = z_0$ (using an iterative solver as it is an implicit equation, $\bar{\mathbf{r}}_z$ denotes the third component of the position vector), the position of a point on the wire's circumference in the cutting plane can be determined.

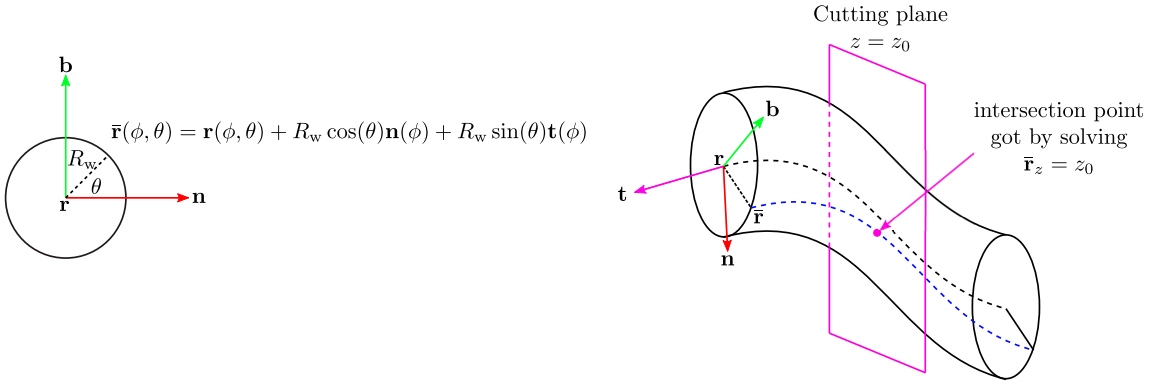

Figure 4: Illustration of the elliptical profile of a pheripheral wire.

After performing the aforementioned procedure for all the peripheral wires in a strand and noting that the cross section of the central wire in the direction of the strand axis is circular, the precise cross sectional shape of a strand is obtained.

Note that when constructing the stand's cross sectional geometry, the following practicality is implemented: The lay radius of the i^{th} layer of wires is reduced by $(i-1)\delta$, where δ denotes a small artificial overclosure. As can be seen in Fig. 5, this practicality creates artificial overclosure between adjacent wires. The purpose of creating such artificial overclosure will be elaborated in the following

section.

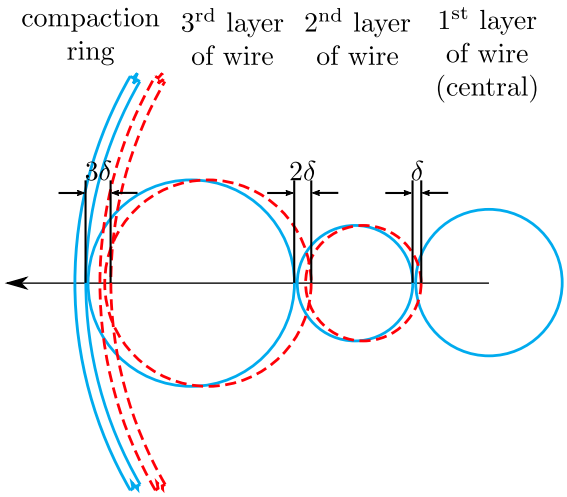

Figure 5: Illustration of artificial overclosure for the strand cross section. The blue solid lines show the geometry before overclosure is introduced and the red dashed lines show the geometry with overclosure incorporated.

2.2 Boundary conditions for compaction

Compaction is applied using somewhat particular boundary conditions, which are described in the current subsection. The amount of compaction is measured in terms of the diameter of the original strand's cross section (d_0) and the diameter of the new, compated strand's cross section, d_{cmp}. With this notation, we quantify the compaction ratio as a normalized reduction of the strand's diameter according to $\frac{d_0 - d_{cmp}}{d_0}$.

Inspired by the physical process of compaction, where the strand/rope is drawn through a circular compaction die, a ring is created that encircles the 2D strand (red in Fig. 6). The inner diameter of the ring is set to $d_0 - 2n\delta$, where δ denotes an artificial overclosure (as mentioned in the last paragraph of the previous subsection), and n denotes the number of layers of wires in the strand (e.g. $n = 3$ for the strand in Fig. 6). Hence, the inner diameter of the compaction ring is reduced by $2n\delta$ so as to create artificial overclosure between the wires and the compaction die. The thickness of the ring has no physical meaning, nor any effect on the results.

Displacements that mimic the compaction process can now be exerted. Specifically, a centripetal

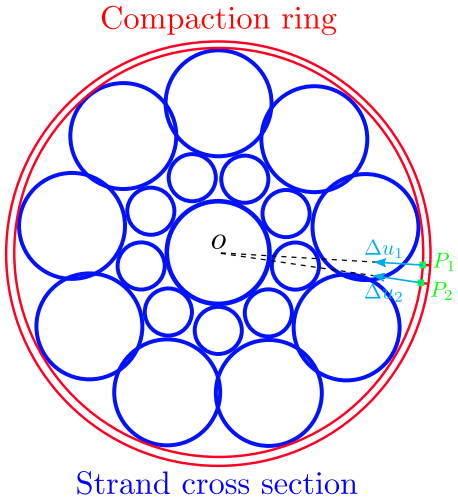

Figure 6: Illustration of the applied boundary conditions in the 2D compaction model: centripetal displacements are prescribed for the entire compaction ring. This is only illustrated for points P_1 and P_2 in the sketch.

displacement with a magnitude of $\frac{d_0 - d_{\text{cmp}}}{2}$ is incrementally prescribed to the entire compaction ring, as shown in Fig 6. The release of the compaction ring after compaction is not incorporated in the simulations, because (1) the elastic release has a negligble influence on the obtained geometry (since most of the compaction-induced deformation is plastic), and (2) the force-equilibrium resulting from the 2D compaction model cannot be incorporated in the 3D model (regardless whether or not elastic release is included or not).

Recall that an artificial overclosure is introduced between neighbouring wires in Section 2.1 and between the wires and the die in this section. This overclosure stabilizes the simulations. The reason for this is that Abaqus incorporates contact constraints from the very start of the simulations when deformable bodies are initially in contact. Hence, a normal stiffness is present between adjacent wires from the very start of the simulation and if frictional contact is modeled, also a tangential stiffness is present. If no overclosure is incorporated, point contact is indeed present in the initial *geometry*, but may not be present in the initial *mesh*. Overclosure thus ensures that initial contact (i.e. an initial stiffness) will always be present between adjacent wires and will be present between more than one contact pair.

2.3 Mesh

We use a four-node bilinear element with plane strain conditions (i.e. the CPE4 element in Abaqus). We use the full integration scheme, because we observed hour-glassing in our preliminary 3D simulations with reduced integration. The compaction ring (with an arbitrary thickness) is discretized with only one element in the radial direction, because the results inside the compaction ring have no physical meaning (since we only use the inner surface of the compaction ring to mimic the boundary conditions occurring during compaction).

2.4 Material model

The isotropic material model for the wires is elastoplastic and uses the logarithmic strain tensor in terms of the left Cauchy-Green deformation tensor, an additive split of the strain in an elastic and a plastic strain, a linear relation between the Cauchy stress tensor and the elastic strain tensor, Von Mises yield criterion, isotropic hardening and an associated flow rule. More details are given in the remainder of this subsection.

We start our more detailed explanation of the constitutive description with the deformation gradient tensor that we denote by $\mathbf{F}$. Using this notation, we write the objective left Cauchy-Green deformation tensor as $\mathbf{B} = \mathbf{F} \cdot \mathbf{F}^T$. The objective, total strain tensor, $\boldsymbol{\epsilon}$, is logarithmically expressed as follows in terms of the left Cauchy-Green deformation tensor:

$$\boldsymbol{\epsilon} = \frac{1}{2}\ln(\mathbf{B}) = \frac{1}{2}\sum_{i=1}^{3}\ln(\beta_i)\tilde{\mathbf{n}}_i\tilde{\mathbf{n}}_i, \tag{4}$$

where β_i and $\tilde{\mathbf{n}}_i$ denote the i^{th} eigenvalue and eigenvector of the left Cauchy-Green deformation tensor, respectively (and the tilde is used to distinguish the eigenvector from the normal vector of the TNB frame). In turn, the strain tensor is additively decomposed in an elastic and plastic strain tensor (superscripts e and p, respectively):

$$\boldsymbol{\epsilon} = \boldsymbol{\epsilon}^e + \boldsymbol{\epsilon}^p. \tag{5}$$

The Cauchy stress tensor, $\boldsymbol{\sigma}$, depends linearly on the elastic strain tensor according to:

$$\boldsymbol{\sigma} = {}^4\mathbf{D}^{el} : \boldsymbol{\epsilon}^e = {}^4\mathbf{D}^{el} : (\boldsymbol{\epsilon} - \boldsymbol{\epsilon}^p)\,, \tag{6}$$

where ${}^4\mathbf{D}^{el}$ denotes the fourth order stiffness tensor, whose components are expressed in terms of one Young's modulus and one Poisson's ratio in case of isotropy as is the case here. With the expression for the Cauchy stress tensor given, its deviatoric part reads:

$$\boldsymbol{\sigma}^{dev} = \boldsymbol{\sigma} - \frac{\mathbf{I} : \boldsymbol{\sigma}}{3}\mathbf{I}, \tag{7}$$

where $\mathbf{I}$ denotes the identity tensor.

We use isotropic hardening and Von Mises yield criterion, γ:

$$\gamma = \sqrt{\frac{3}{2}\boldsymbol{\sigma}^{dev} : \boldsymbol{\sigma}^{dev}} - \sigma^{y0} - H(\epsilon_{pl}^{eq})^m, \tag{8}$$

where material parameters σ^{y0}, H, m denote the initial yield stress, the hardening modulus and a dimensionless exponential hardening parameter. Furthermore, ϵ_{pl}^{eq} denotes the equivalent plastic strain, also known as the cumulative plastic strain.

If the yield criterion is exceeded, plastic deformation will grow according to the following associated flow rule:

$$\dot{\boldsymbol{\epsilon}}^p = \dot{\epsilon}_{pl}^{eq} \frac{\partial \gamma}{\partial \boldsymbol{\sigma}}. \tag{9}$$

The Karush-Kuhn-Tucker conditions formally express the conditions of the yield criterion, the growth of the equivalent plastic strain and the relation between the two:

$$\gamma \leq 0, \qquad \dot{\epsilon}_{pl}^{eq} \geq 0, \qquad \dot{\epsilon}_{pl}^{eq}\gamma = 0. \tag{10}$$

As a last remark, we want to emphasize that the material description of the compaction ring is completely irrelevant. However, because Abaqus requires some input material definition for the ring (even though its response is fully governed by Dirichlet boundary conditions to save time), we use the elastic variant of the model described in this subsection (by setting the initial yield stress to a significantly large value).

2.5 Contact formulation

In this subsection, we discuss some details of the employed contact description. In summary, we can state that we use a master-slave approach where the penalty approach is used both for the normal contact (to prevent penetration) and for frictional sliding in tangential direction. Frictional sliding is modeled using Coulomb's friction law.

Normal contact

Contact is enforced using a node-to-surface (slave-master) approach (albeit a wide range of more advanced contact frameworks exist these days, see e.g. [11, 12, 16]). This entails that a node of the slave surface experiences a force that aims to minimize the penetration of the slave node in the master surface. Since the contact conditions are enforced using the penalty approach, the repulsive force in the simplest case is written as:

$$\mathbf{f}_N = k_N \mathbf{g}_N, \tag{11}$$

where k_N and $\mathbf{g}_N$ denote the penalty stiffness and the gap vector, respectively. Subscript N is included to denote that these symbols are related to normal contact that aims to minimize penetration (Below we will use subscript T to denote tangential sliding of the slave node over the master surface, which may come with frictional forces.)

In theory, one wants to use a large penalty stiffness, k_N, in order to minimize the amount of penetration. In practise however, this entails that Newton's method will not converge. One thus starts with a small penalty stiffness and continuously updates it during the course of simulation: the penalty stiffness will be increased if a maximum allowable penetration is exceeded, or reduced when a minimum allowable penetration is reached (which occurs during unloading of the respective slave point).

Gap vector $\mathbf{g}_N$ is defined as the vector between the slave node and the point of the master surface nearest to the slave node (the projection point). Only if the slave node penetrates the master surface, Eq. (11) is incorporated. If no penetration occurs, Eq. (11) is simply ignored.

Eq. (11) defines the simplest form of the normal contact force. One may also define the normal

force quadratically in terms of the magnitude of the gap vector for small penetrations [19] and resort to the linear expression of Eq. (11) for larger penetrations. Which expression Abaqus exploits is not clear to us from the documentation, nor the heuristics to update the penalty stiffness and the automatic choice for the maximum allowable penetration and the minimum allowable penetration.

Frictional sliding

Frictional sliding of the slave node over the master surface is modeled using Coulomb's friction law. Central in Coulomb friction is the following stick-slip condition:

$$\mathbf{f}_T \leq \mu \|\mathbf{f}_N\| \mathbf{n}_T, \tag{12}$$

where $\mathbf{f}_T$ denotes the tangential force vector due to friction, $\|\bullet\|$ the l^2-norm, μ the friction coefficient, $\mathbf{f}_N$ the normal force vector of Eq. (11), and $\mathbf{n}_T$ the unit vector in the tangential direction in which sliding occurs. In case the tangential force remains below $\mu\|\mathbf{f}_N\|$, the slave node will stick to the current location at the master surface. If this is not the case, the slave node will slide over the master surface.

In Abaqus, this behaviour is again implemented with a penalty spring that (roughly speaking) acts between the projection point of the previous increment and the current projection point. This penalty spring is in essence an elastoplastic spring with no hardening modulus (i.e. perfect plasticity), with a small elastic domain and a yield force that is not constant, but equals $\mu\|\mathbf{f}_N\|$. The advantage of using this penalty description instead of a Lagrange multiplier (which is also an option in Abaqus) is an improved robustness for Newton's method.

Again, we have not been able to find some details in the Abaqus documentation. This includes the automatic selection for the value of the tangential penalty spring (which is not updated during the course of a simulation, in contrast to normal penalty stiffness k_N), and the exact definition of the sliding distance.

Practicalities

Details of the use of the contact formulation for the 2D compaction simulations are listed in Table 1. In principle, our aim was not to use friction at all, since (1) the compaction process involves substantial lubrication, and (2) the friction coefficient is hard to experimentally determine. However, without the use of friction, the simulations did not converge. We therefore included frictional contact between the compaction ring and its adjacent wires and this was sufficient to make the simulations robustly converge.

<table>
<tr><th>Type of contact pair</th><th colspan="2">Selection of contact pair</th><th>Normal behavior</th><th>Tangent behavior</th></tr>
<tr><td></td><td>Master surface</td><td>Slave surface</td><td></td><td></td></tr>
<tr><td>ring-to-wire contact</td><td>Inner cirfumference of the die</td><td>Cirfumferences of wires on the outmost layer of the strand</td><td rowspan="3">Penetration of the slave surface into the master surface minimized by penalty method, transfer of tensile stress across the interface not allowed.</td><td>Finite sliding with friction coefficient of 0.3.</td></tr>
<tr><td rowspan="2">inter-wire contact</td><td>Circumference of a wire</td><td>Circumference of a neighbouring wire in the same layer</td><td rowspan="2">Finite sliding frictionless</td></tr>
<tr><td>Circumference of a wire</td><td>Circumference of a wire in the neighbouring layer</td></tr>
</table>

Table 1: Configuration of contact behavior in the 2D compaction model.

2.6 Solution scheme

The 2D compaction simulations are constructed in an implicit dynamical setting in order to avoid singularities of the stiffness matrices of quasi-static settings. However, the singularities resulting from quasi-static settings can be circumvented by preventing slipping for contact, which can be achieved by assuming an infinite coefficient of friction (see Appendix A). The backward Euler scheme is used for the temporal discretization. In the following, key concepts in the adopted implicit dynamic formulation are revisited. The length of a time step is denoted by Δt. A quantity that must be computed (during the new time increment) is denoted with subscript $t+\Delta t$ and a converged quantity

at the previous time increment is denoted with superscript t. For more details, interested readers are referred to [25].

In the adopted formulation, the governing equations (after spatial discretization, but before temporal discretization) can be written as follows:

$$\underline{\underline{M}}\,\underline{\ddot{u}} + \underline{f}(\underline{p}, \underline{u}) = \underline{f}_{\text{ext}}, \tag{13}$$

with $\underline{u}$, $\underline{\dot{u}}$ and $\underline{\ddot{u}}$ denote denoting the nodal displacements, velocities and accelerations, respectively. $\underline{\underline{M}}$ denotes the lumped mass matrix (which is diagonal) and $\underline{f}(\underline{p}, \underline{u})$ denotes column with non-linear forces associated with the material description and the contact formulation. $\underline{p}$ denotes the history variables, i.e. the plastic strain tensor and the equivalent plastic strain in each quadrature point, as well as the tangential sliding distance due to frictional surface sliding. The column with externally applied forces (including externally applied body forces) is denoted by $\underline{f}_{\text{ext}}$.

Backward Euler, as applied in this contribution, temporally discretizes kinematic quantities as follows:

$$\underline{u}^{t+\Delta t} = \underline{u}^{t} + \Delta t\ \underline{\dot{u}}^{t+\Delta t} \tag{14}$$

and

$$\underline{\dot{u}}^{t+\Delta t} = \underline{\dot{u}}^{t} + \Delta t\ \underline{\ddot{u}}^{t+\Delta t}. \tag{15}$$

In the backward Euler scheme, the governing equations of Eq. (13) are then written as follows:

$$\underline{\underline{M}}\,\underline{\ddot{u}}^{t+\Delta t} + \underline{f}(\underline{p}^{t+\Delta t}, \underline{u}^{t+\Delta t}) = \underline{f}_{\text{ext}}^{t+\Delta t}, \tag{16}$$

Inserting the temporal discretization of Eqs. (14) and (15) in the governing equations, yields the following system of non-linear equations that must be solved each time increment:

$$\frac{1}{\Delta t^2}\underline{\underline{M}}\,\underline{u}^{t+\Delta t} + \underline{f}(\underline{p}^{t+\Delta t}, \underline{u}^{t+\Delta t}) = \underline{f}_{\text{ext}}^{t+\Delta t} + \frac{1}{\Delta t^2}\underline{\underline{M}}\,\underline{u}^{t} + \frac{1}{\Delta t}\underline{\underline{M}}\,\underline{\dot{u}}^{t}, \tag{17}$$

which is solved using Newton's method, for which the following linearization is required:

$$\left(\frac{1}{\Delta t^2}\underline{\underline{M}} + \left.\frac{\partial \underline{f}}{\partial \underline{u}}\right|_{\tilde{\underline{p}}^{t+\Delta t},\tilde{\underline{u}}^{t+\Delta t}}\right)\Delta \underline{u}^{t+\Delta t} = \underline{f}_{\text{ext}}^{t+\Delta t} - \underline{f}(\tilde{\underline{p}}^{t+\Delta t},\tilde{\underline{u}}^{t+\Delta t}) + \frac{1}{\Delta t^2}\underline{\underline{M}}\,\underline{u}^t + \frac{1}{\Delta t}\underline{\underline{M}}\,\dot{\underline{u}}^t - \frac{1}{\Delta t^2}\underline{\underline{M}}\,\tilde{\underline{u}}^{t+\Delta t}, \tag{18}$$

where $\tilde{\underline{u}}^{t+\Delta t}$ and $\Delta \underline{u}^{t+\Delta t}$ denote the estimate of the current nodal displacements and the correction to the estimate, respectively. $\frac{\partial \underline{f}}{\partial \underline{u}}$ denotes a matrix with a derivatives, in which a component on row i, column j is calculated as follows:

$$\left(\frac{\partial \underline{f}}{\partial \underline{u}}\right)_{ij} = \frac{\partial (\underline{f})_i}{\partial (\underline{u})_j}. \tag{19}$$

Furthermore, a return mapping algorithm is used to calculate the plastic strain tensor and the equivalent plastic strain in $\tilde{\underline{p}}^{t+\Delta t}$, that are associated with the estimate of the current nodal displacements, $\tilde{\underline{u}}^{t+\Delta t}$.

2.7 Postprocessing of 2D compaction model

Upon completion of the compaction simulation, two types of results are extracted: 1) the geometrical shapes of the compacted wire cross sections, and 2) the field of the equivalent plastic strain of each wire cross section. The former can be easily obtained by extracting the new locations of the finite element nodes on the wires' circumference. The latter takes the form of a 2D point cloud. Specifically, the 2D coordinates (x, y) and the corresponding equivalent plastic strain, $\epsilon_{pl}^{eq}(x, y)$, are recorded for each integration point.

As will be elaborated in the following section, the profiles of the compacted wire cross sections are used to construct the 3D model for the compacted strand. The 2D point cloud of equivalent plastic strains is used to set the initial field of work hardening in the 3D strand model.

3 3D strand model

This section discusses the 3D finite element model to subject the strand to axial tension after compaction is simulated. Section 3.1 details the finite element model, based on the compaction

results of the compaction model. Section 3.2 focuses on the projection of the 2D point cloud of equivalent plastic strains, computed by the compaction model, onto the 3D strand model.

3.1 Finite element model

The 3D model is very similar to the 2D compaction model, with a few exceptions. The issues that remain the same or are trivial (e.g. the material model, the contact definition, removal of the compaction ring) are not discussed again. Instead, we only focus on the interesting differences with respect to the 2D compaction model.

In a straight strand, the peripheral wires are helices, twisted around the axis of the strand. Therefore, the 3D geometry of the compacted strand can be established by extruding the 2D compacted strand cross section along the strand axis, whilst at the same time rotating the strand's cross section around the strand axis. After extruding (whilst rotating) the cross section for a distance of lay length L_{lay}, the cross section has rotated 2π and the cross section finds itself in the starting orientation.

Once the 3D strand geometry is obtained from extrusion, it is meshed using trilinear hexahedrons with eight quadrature points (i.e. the C3D8 element in Abaqus). The reason of using hexahedral mesh is that in 3D model problems, hexahedral element is more preferential compared to tetrahedral elements in terms of accuracy [25]. Specifically, an approximate element size is given by the user to generate uniform hexahedral mesh for the 3D strand model. Important to realize is that the mesh is cross-sectionally not the same as the 2D mesh of the compaction simulation and that the elements in the direction of the strand's axis have the same length (see Fig. 7).

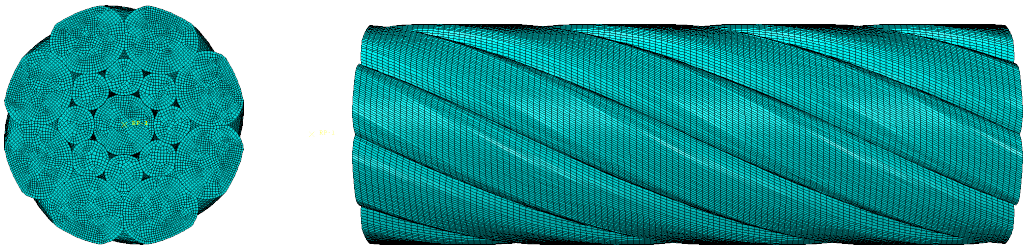

(a) Cross sectional view. (b) Side view.

Figure 7: The mesh employed for the 17S strand.

The 3D model is only investigated to predict the tension response. Tension is prescribed by prescribing all the displacement components of all the FE nodes of the two outer strand cross sections. The implicit simulations are quasi-static and solved using Newton's method, because zero-energy modes do not occur thanks to the prescribed boundary conditions. In other words, we treat Eqs. (12), (15-17), but we ignore the mass matrices, the velocities, the accelerations and the contributions of body forces in $\underline{f}_{\text{ext}}$.

It may also be noted that we have performed the 3D simulations using the dynamic setting of Eqs. (12), (15-17), but that hardly any differences in the results were observed.

3.2 Transfer of compaction results to 3D model

A crucial, if not the most important, setup of the finite element model for the 3D strand is the initiation of equivalent plastic strain in the integration points. This is intended to mimic compaction induced work hardening in the 3D strand model. Yet, only the field of equivalent plastic strains over the 2D compacted strand cross section in the form of a 2D point cloud is available. Thus, a projection between the 2D model and the 3D model in terms of the equivalent plastic strain needs to be undertaken. Fig. 8 illustrates the projection procedure that is proposed and adopted in the present work.

Note that in the penultimate step of the flow chart in Fig. 8, the equivalent plastic strain of the target integration point is set to equate the counterpart of the nearest point in the 2D point cloud. Such an approximation may be debatable as one may favor the introduction of an interpolation algorithm to achieve local regression. From the authors' perspective, since relatively refined meshes are adopted in the 2D compaction model, which consequently leads to large number of data points (at the integration points) in the 2D point cloud, the authors have chosen to circumvent the extra complexity of an interpolation algorithm.

The complete modeling and analysis procedure for a compacted strand is summarized in Fig. 9. For better clarity, red and blue dashed boxes are included in Fig. 9 to highlight the parts of work pertaining to the 2D compaction model of Section 2 and the 3D strand model of Section 3.

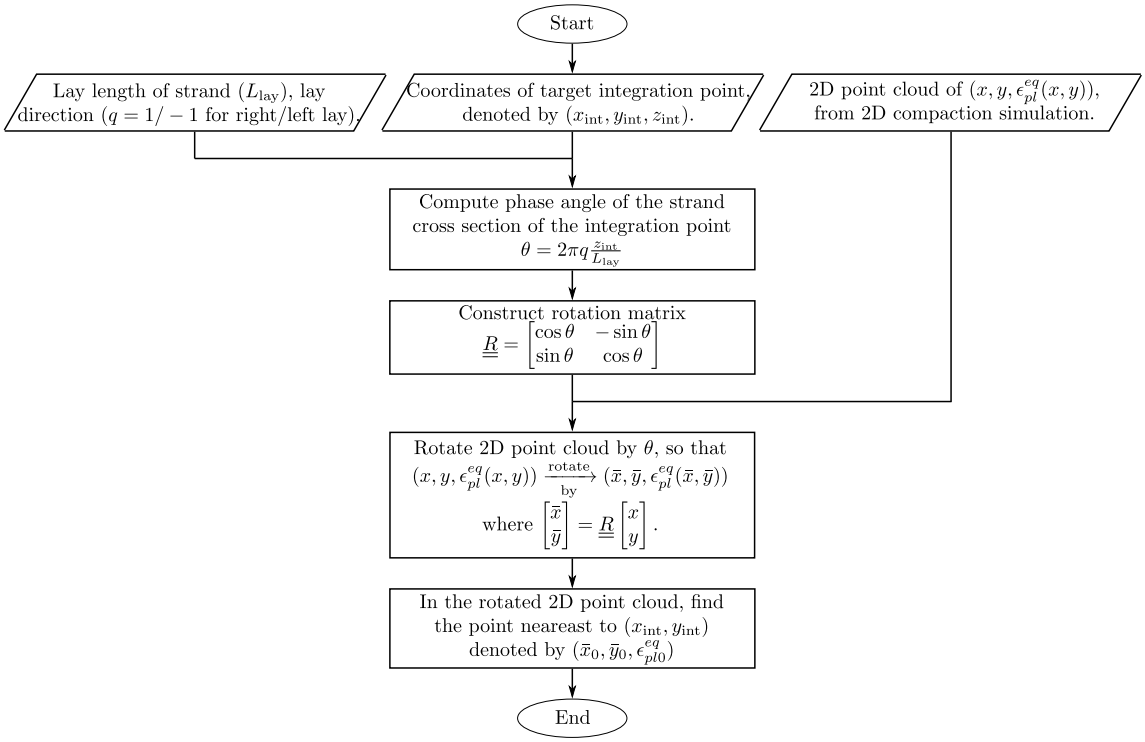

Figure 8: Flow chart of projecting the 2D point cloud of equivalent plastic strains onto integration points in 3D strand model.

4 Results

In this section, the modeling is applied to two benchmark strand designs: a 1+6 strand and a strand design coined 17S. The cross sections of these strands are sketched in Fig. 10. The geometrical information of these two strand designs is listed in Table 2. For each strand design, two lay lengths, i.e. 27.5 mm and 47.5 mm, are considered. Moreover, for each strand design two cases are considered: the uncompacted case and a compacted case. For the compacted cases, a compaction ratio of 8.6% is investigated for the 1+6 strand, and a compaction ratio of 7.2% for strand design 17S. These compaction ratios are chosen by our collaborators at Kiswire Inc. when carrying out their experimental manufacturing and testing. All considered cases are summarized in Table 3.

In terms of the all the experiments listed in Table 3, they are carried out at the KV R&D Center GmbH (*https://verope.com/kv-rd-en/*) in Germany.

It is worth noting that in groups 3, 4, 7 and 8 of Table 3, two numerical simulations are performed

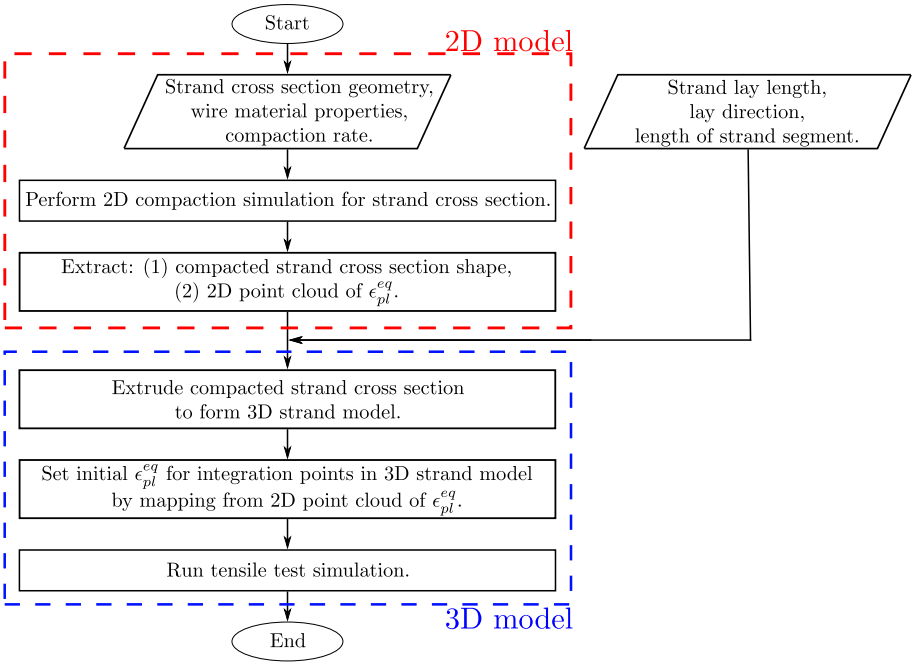

Figure 9: Flow chart of the modelling approach.

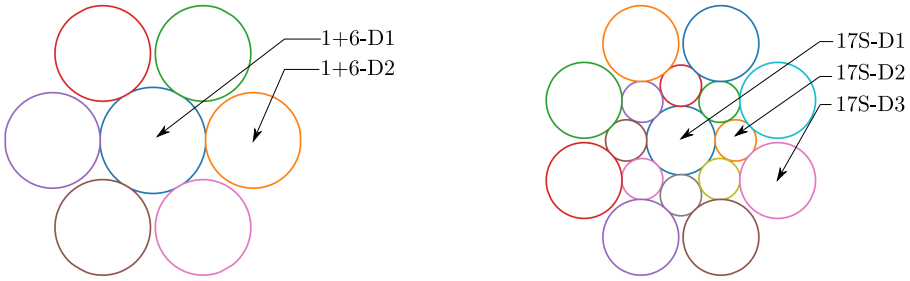

(a) Strand design 1+6.

(b) Strand design 17S.

Figure 10: Studied strand designs. Encoding of wires is annotated.

per group. In one case, only the shape/geometry of the compacted strand cross section is transfered to the 3D strand model, and the field of compaction induced plasticity is not projected onto the 3D model. In the other case, both the shape/geometry and the plasticity predicted by the compaction simulation are transfered to the 3D model.

In all the simulations, identical seed spacings in the strand cross section and along the strand

Strand design	Uncompacted strand diameter [mm]	Wire identifier	Wire diameter [mm]
1+6	5.02	D1	~ 1.8
		D2	~ 1.6
17S	5.02	D1	~ 1.2
		D2	~ 0.7
		D3	~ 1.3

Table 2: Diameters of wires and strands.

Group	Strand design	Lay length (mm)	Compaction rate (%)	Source of tensile result
1	1+6	27.5	0.0	Exp 1, Exp 2 Num
2	1+6	47.5	0.0	Exp 1, Exp 2 Num
3	1+6	27.5	8.6	Exp 1, Exp 2 Num, Cmp Num, Cmp + Hard
4	1+6	47.5	8.6	Exp 1, Exp 2 Num, Cmp Num, Cmp + Hard
5	17S	27.5	0.0	Exp 1, Exp 2 Num
6	17S	47.5	0.0	Exp 1, Exp 2 Num
7	17S	27.5	7.2	Exp 1, Exp 2 Num, Cmp Num, Cmp + Hard
8	17S	47.5	7.2	Exp 1, Exp 2 Num, Cmp Num, Cmp + Hard

Table 3: Summary of the investigated setups. Abbreviations: Exp–experimental test, Num– numerical simulation, Cmp–compacted geometry, Hard–work hardening inherited from the compaction results. Exp 1 and Exp 2 mean two tests are conducted for the same setting so as to reduce variance.

axis are adopted. In this way, the mesh density becomes a control variable and the comparability among the numerical models is justified. Particularly, the mesh seed spacing in the strand cross section is chosen as 0.05 mm. The seed spacing along the strand axis is set to 0.1 mm. Fig. 7 shows a typical mesh for the compacted 17S strand with a lay length of 27.5 mm.

This section is organized as follows: In Section 4.1, tensile test results of single wires that

comprise the to-be-studied strands are fitted to define material behaviors for the finite element models. In Section 4.2, 2D compaction simulations are performed for the benchmark strand designs. The geometry and the plastification of the strand cross sections serve as the basis to construct the 3D strand model in the subsequent section. In Section 4.3, numerical tensile tests are carried out on the uncompacted strands and the compacted strands. In the case of the compacted strand, the geometry of the strand will be established using the deformed strand profile from the 2D compaction simulation in Section 2. Nevertheless, in order to show the necessity of accounting for the compaction induced work hardening, two scenarios will be considered. In one scenario, the strand model will be initialized using the plastic strain field from the 2D compaction simulation of Section 2, while in the other, no initialization of plastic strain will take place.

4.1 Parameter calibration

Tensile tests are conducted for each type of wire in the two strand designs. The nominal/engineering stress–strain curves of the tensile tests (for which constant length and diameter of the sample are assumed throughout the whole experiment) are transformed into true stress–strain relations using the following transformations:

$$\epsilon = \ln(1 + \epsilon_{\text{nom}}), \tag{20}$$

$$\sigma = \sigma_{\text{nom}}(1 + \epsilon_{\text{nom}}), \tag{21}$$

where $(\sigma_{\text{nom}}, \epsilon_{\text{nom}})$ and (σ, ϵ) denote the nominal and true stress and strain, respectively.

The true stress–strain curves are plotted in Fig. 11a for the wires of the 1+6 strand and in Fig. 11b for the wires of strand design 17S. The figures show a satisfying match between the experimental and identified stress-strain relations.

4.2 Compaction results

Compaction simulations are performed using the modeling techniques elaborated in Section 2. Fig. 12 shows the strand cross sections before the compaction simulations. In particular, the difference between using elliptical cross section and assuming circular cross section (which is a frequently

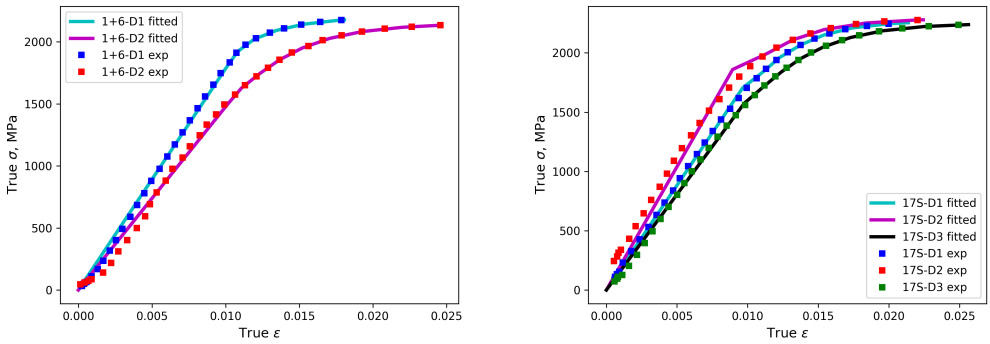

(a) Wires of the 1+6 strand.

(b) Wires of the 17S strand.

Figure 11: Experimental and calibrated stress-strain relations of the base materials of the different wires in the 1+6 strand (left) and strand 17S (right).

adopted in industrial practice) for peripheral wires is highlighted in Fig. 12. Clearly and logically, the difference diminishes as the lay length increases.

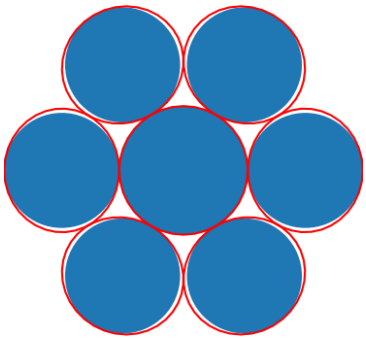

(a) Strand 1+6 with lay length of 27.5 mm.

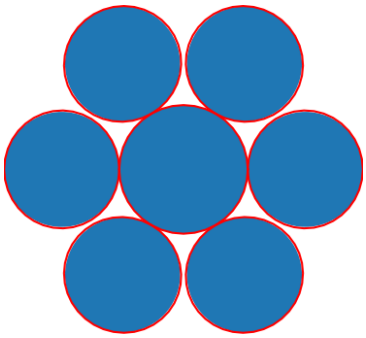

(b) Strand 1+6 with lay length of 47.5 mm.

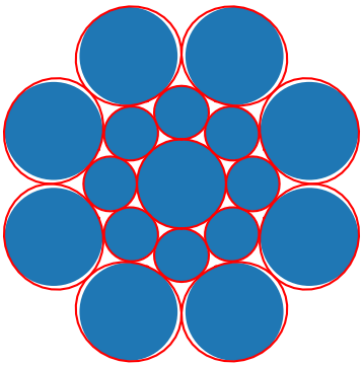

(c) Strand 17S with lay length of 27.5 mm.

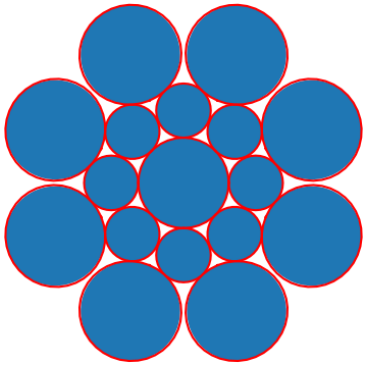

(d) Strand 17S with lay length of 47.5 mm.

Figure 12: The initial cross sections for different lay factors in red, compared to perfectly circular wires in blue.

Figs. 13c, 13d, 14c and 14d show the wire profiles and the predicted fields of equivalent plastic strains after compaction for strand design 1+6 and 17S, respectively. As can be seen, for the outmost wires, plasticity initiates from the inter-wire contact zone and the ring-to-wire contact zone, before traversing the wire cross section and forming band shaped patterns. For the wires that are not situated on the outmost layer, plasticity, if there is any, is constrained to the inter-wire contact zone.

An interesting result, possible thanks to the consideration of elliptical wire cross sections in the strand's initial cross section and the different number of layers of wires, is that for the 1+6 strand, the peak plastic strain for the smaller lay length is lower than that for larger lay length, while the opposite trend is observed for the 17S strand.

The cross sections of the manufactured strands before and after compaction are also presented in Figs. 13a and 13b for strand design 1+6 and in Figs. 14a and 14b for strand design 17S. We can

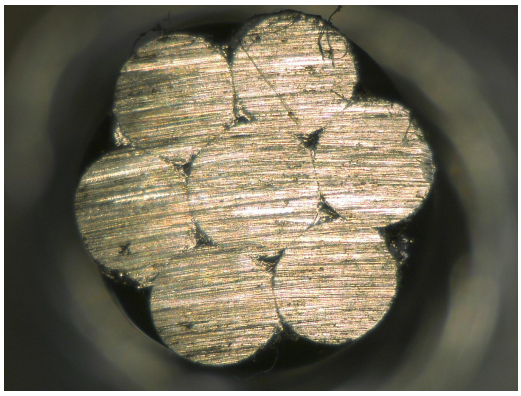

(a) No compaction, lay length=27.5 mm.

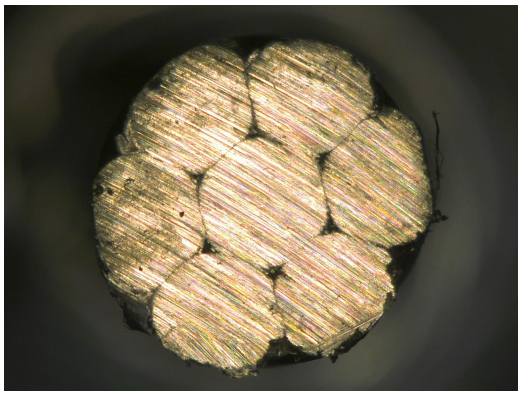

(b) Compaction ratio = 8.6%, lay length=27.5 mm.

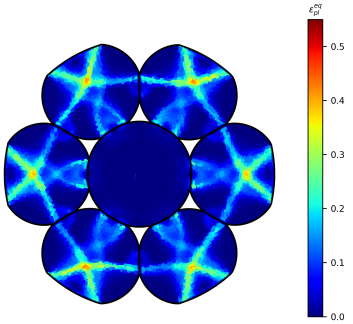

(c) Compaction ratio = 8.6%, lay length=27.5 mm.

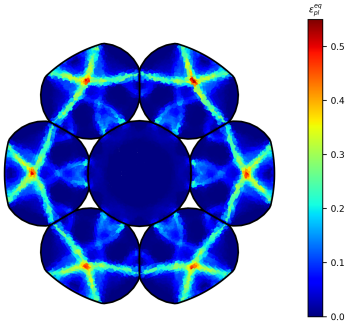

(d) Compaction ratio = 8.6%, lay length=47.5 mm.

Figure 13: Compaction for 1+6 strand: experimental and numerically predicted cross sections. In the bottom figures, green shows the predicted equivalent plastic strain.

make two important observations. First, the wires in the initial strand designs (without compaction, Figs. 13a and 14a) have already undergone plastic deformation during the twisting of the wires into the strand. This plasticity is also not incorporated in our modelling approach. Second, the compaction has clearly made the strand's circumference more round and has compressed the wires to each other. This is well predicted by the compaction model.

4.3 Tension results

3D strand models are established using the 2D compacted shapes of the strand cross sections from the previous section. Convergence analysis shows that half the lay length of the strand suffices to

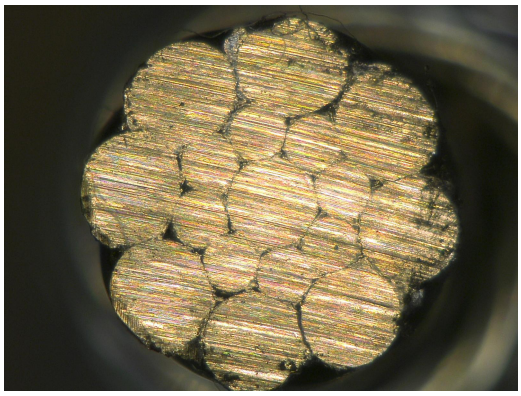

(a) No compaction, lay length=27.5 mm.

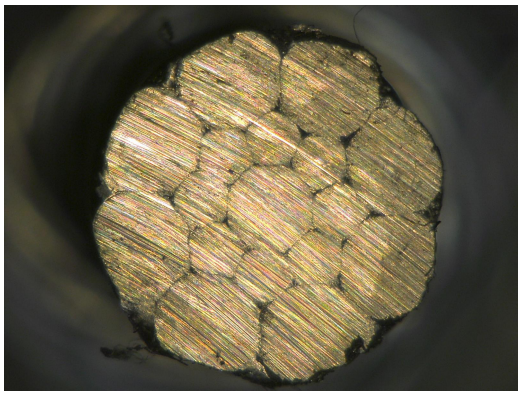

(b) Compaction ratio = 7.2%, lay length=27.5 mm.

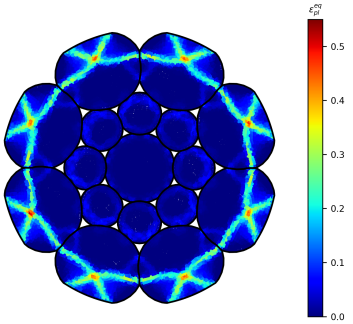

(c) Compaction ratio = 7.2%, lay length=27.5 mm.

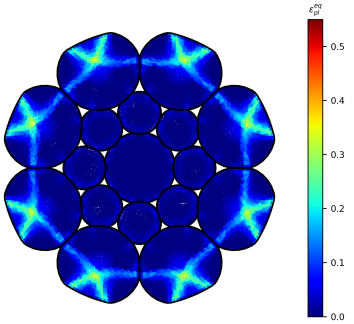

(d) Compaction ratio = 7.2%, lay length=47.5 mm.

Figure 14: Compaction for 17S strand: experimental and numerically predicted cross sections. In the bottom figures, green shows the predicted equivalent plastic strain.

generate converged tensile response. Therefore, the length of strand to be modeled is set to half the lay length of the strand.

4.3.1 Strand design 1+6

Fig. 15 shows the initial 3D strand model for strand design 1+6 with a lay length of 47.5 mm, prior to tensile loading (in case compaction induced work hardening is inherited from the 2D compaction simulation). The contour in Fig. 15 illustrates the spatial distribution of equivalent plastic strains in the strand. A similar pattern of plastic deformation was reported in [34] where the compaction of a 1+6 strand was modeled by drawing the 3D strand through a circular die.

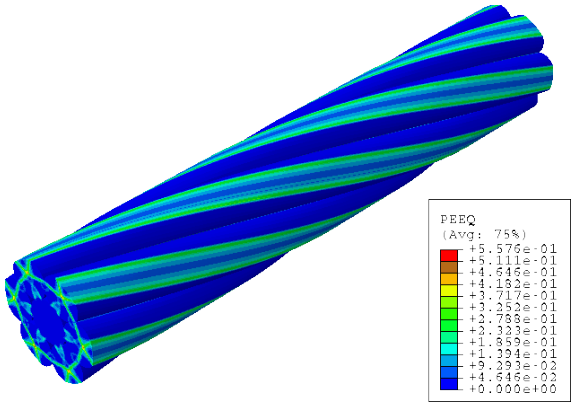

Figure 15: 1+6 strand: the 3D model for a lay length of 47.5 mm prior to tensile loading. Half a lay length is modeled. The distribution of the equivalent plastic strain (a.k.a. PEEQ) from Fig. 13c is included in the 3D model.

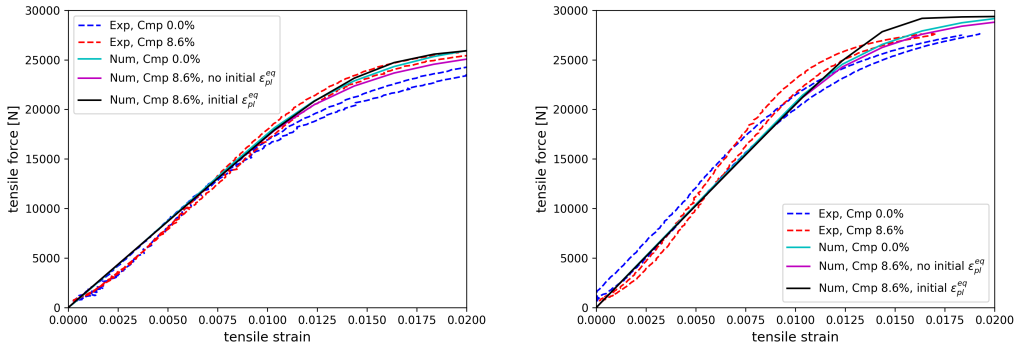

(a) Lay length = 27.5 mm.

(b) Lay length = 47.5 mm.

Figure 16: 1+6 strand: The forces numerically predicted (solid) and experimentally obtained (dahsed) as a function of the applied engineering tensile strain. Note that each real-world strand is tested twice.

The tensile responses of the 1+6 strands, both experimentally measured and numerically predicted, are summarized in Fig. 16. The predicted curves do not show a perfect match with the experimental curves, but the match is nevertheless satisfactory in the authors' opinion. It is worth noting that in Fig. 16, during the elastic loading stage, the predicted curves corresponding to the compacted strands (with and without initial ϵ_{pl}^{eq}) exhibit the same slope. The reason is that each pair of strands (with and without ϵ_{pl}^{eq}) is geometrically the same, and initially no plastic strain is present (only the value of ϵ_{pl}^{eq} differs after all).

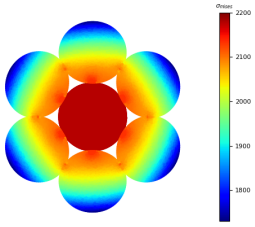

(a) Uncompacted strand, lay length=27.5 mm.

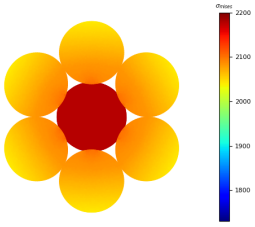

(b) Uncompacted strand, lay length=47.5 mm.

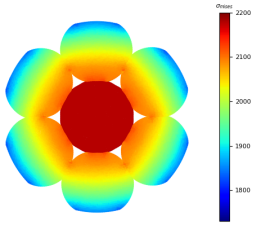

(c) Compacted strand without inherited hardening, lay length=27.5 mm.

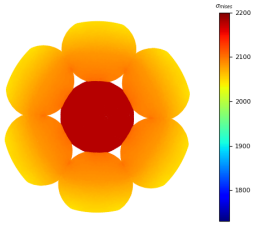

(d) Compacted strand without inherited hardening, lay length=47.5 mm.

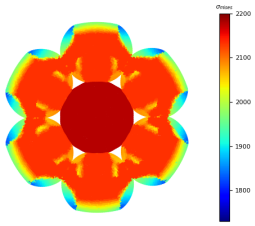

(e) Compacted strand with inherited hardening, lay length=27.5 mm.

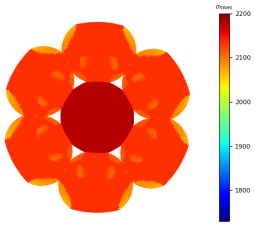

(f) Compacted strand with inherited hardening, lay length=47.5 mm.

Figure 17: 1+6 strand: Predicted Von Mises stresses.

The fact that the slope of the numerical uncompacted strand is also the same as those of the two numerically compacted strain is somewhat surprising, since the geometries are not similar. This may indicate (together with Fig. 20) that the compaction model may be ignored if one is solely interested in determining the initial tensile stiffness of a strand.

On the other hand, if one is interested in more than the elastic stiffness, the compaction model does affect the result. The reason is that one can clearly see a different response when plastic deformation occurs: plastic deformation occurs at different strains in the different models. Furthermore, the curves show that compaction induced work hardening provides completely different results and must be incorporated. If it is not incorporated, the uncompacted model predicts higher force than

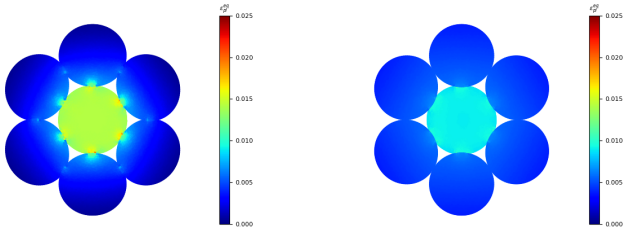

(a) Uncompacted strand, lay length=27.5 mm. (b) Uncompacted strand, lay length=47.5 mm.

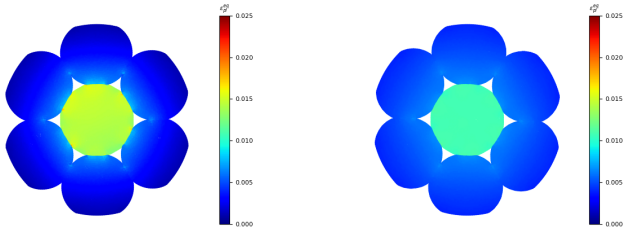

(c) Compacted strand without inherited hardening, lay length=27.5 mm. (d) Compacted strand without inherited hardening, lay length=47.5 mm.

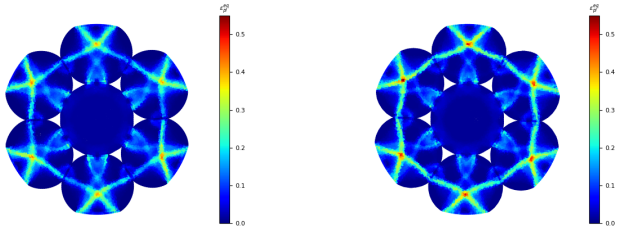

(e) Compacted strand with inherited hardening, lay length=27.5 mm. (f) Compacted strand with inherited hardening, lay length=47.5 mm.

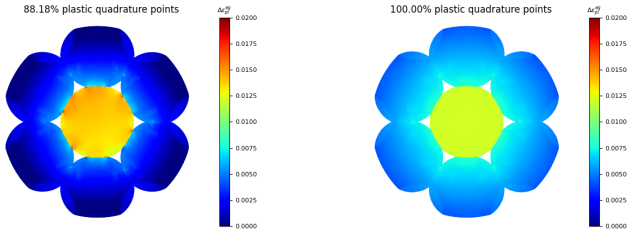

(g) $\Delta\epsilon_{pl}^{eq}$, lay length=27.5 mm. (h) $\Delta\epsilon_{pl}^{eq}$, lay length=47.5 mm.

Figure 18: 1+6 strand: Predicted equivalent plastic strains (a.k.a. PEEQ). The bottom two images show the difference of the equivalent plastic strain predicted after compaction and after tensile loading for the case where the equivalent plastic strain in the 3D model is inherited from the 2D compaction model.

the compacted model, which is the opposite trend of the experimental curves.

Figs. 17 and 18 show the fields of von Mises stresses and equivalent plastic strains for the central

cross sections of the 3D strands at the end of tensile loading. Particularly, the field of incremental equivalent plastic strain as a result of the tensile test for the central cross section is plotted in Figs. 18g and 18h, respectively. It is obtained by subtracting the equivalent plastic strain that is inherited from the 2D compaction model from the equivalent plastic strain at the end of tensile loading.

The results not only show different predictions for the different lay lengths, they also show different fields predicted for the uncompacted model, the compacted model without inheritance of compaction induced work hardening and the compacted model with inheritance of compaction induced work hardening.

Finally, it is worth noting that the fields predicted for the large lay length (right diagrams in Fig. 17 and 18) show larger quantities (i.e. von Mises stress or the equivalent plastic strain) and less spatial fluctuation of the quantities than those predicted for the small lay length (left diagrams in Fig. 17 and 18). The reason for this is that the larger the lay length, the more the strand approaches a bundle of parallel wires. Consequently, for an increase of the lay length, (1) the quantity will be larger (for the same applied strain), and (2) the spatial distribution of the quantity is more homogeneous. The same trend can be observed in the next subsection for which a 17S (1+8+8) strand is analyzed.

4.3.2 Strand design 17S

Fig. 19 shows the initial 3D strand model for design 17S with a lay length of 27.5 mm, prior tensile loading (in case compaction induced work hardening is inherited from the 2D compaction simulation). The contour in Fig. 19 illustrates the spatial distribution of equivalent plastic strains in the strand.

The experimental and predicted tensile responses for strand design 17S are presented in Fig. 20. We make several observations. The first observation is that the numerical curves for the small lay length (left diagram) match the experimental curves less accurately than for the large lay length (right diagram), as well as for all 1+6 strand designs. We expect that this mismatch is caused by the fact that more and thinner wires are present than in the 1+6 strand design and because more plasticity has occurred to manufacture the small lay length. We expect that because of this, the

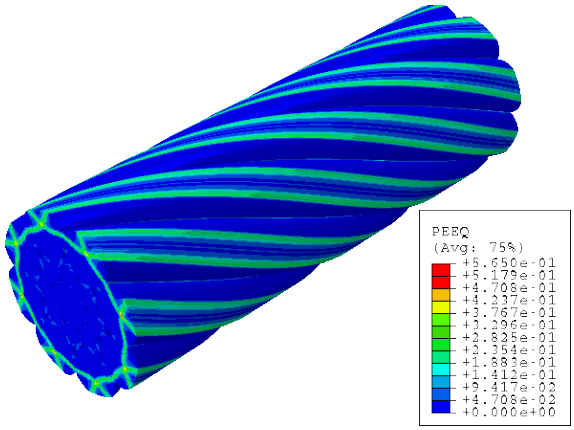

Figure 19: Strand 17S: The initial 3D model for a lay length of 27.5 mm prior to tensile loading. Half a lay length is modeled. The distribution of the equivalent plastic strain (i.e. PEEQ) from Fig. 14c is included in the 3D model.

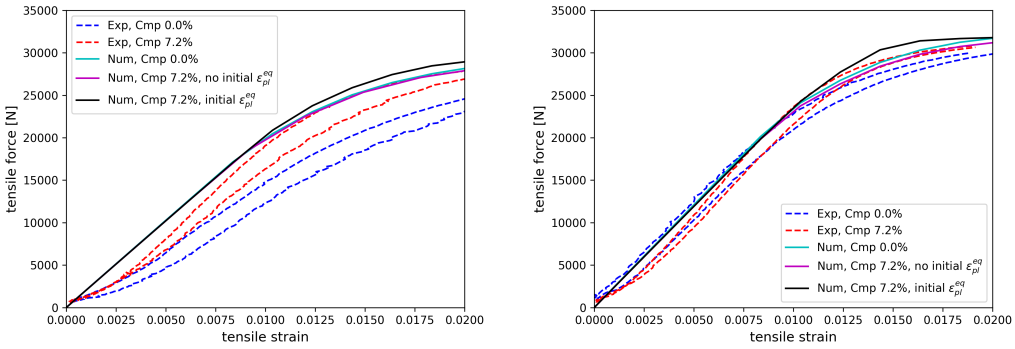

(a) lay length=27.5 mm.

(b) lay length=47.5 mm.

Figure 20: Strand 17S: the forces numerically predicted (solid) and experimentally obtained (dahsed) as a function of the applied engineering tensile strain. Note that each real-world strand is tested twice.

wires in the strand are not perfectly attached, whereas in the model the orientation of each wire and connection is to the adjacent wires is perfect and hence, the predicted force is larger. Nevertheless, the fact that the model does not include plastic deformation induced by the manufacturing of the strand (in which the wires are twisted together) will also have a substantial influence.

Even though the match between the experimental and predicted force-strain results is not as good as for the 1+6 strands, the trends of the predictions remain the same: the compacted model with inheritance of compaction induced work hardening predicts a larger force than the uncompacted

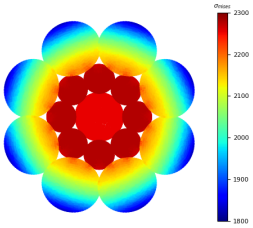

(a) Uncompacted strand, lay length=27.5 mm.

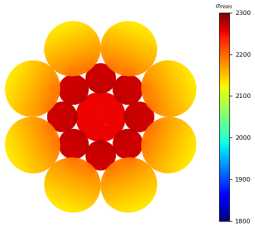

(b) Uncompacted strand, lay length=47.5 mm.

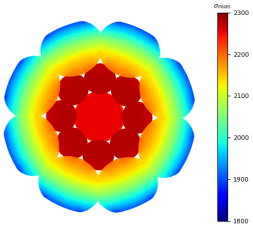

(c) Compacted strand without inherited hardening, lay length=27.5 mm.

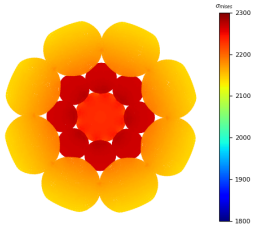

(d) Compacted strand without inherited hardening, lay length=47.5 mm.

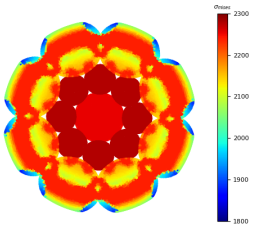

(e) Compacted strand with inherited hardening, lay length=27.5 mm.

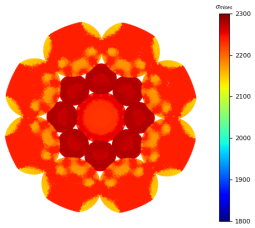

(f) Compacted strand with inherited hardening, lay length=47.5 mm.

Figure 21: Strand 17S: Predicted Von Mises stresses.

model. The same trend is also seen in the experimental results. On the other hand, the compacted model without inheritance of the compaction induced work hardening predicts a small force than the uncompacted model, resulting in the conclusion (the same as for the 1+6 designs) that it is crucial to inherit compaction induced work hardening.

Figs. 21 and 22 show the fields of von Mises stress and equivalent plastic strains for the central cross sections of the 3D strands at the end of tensile loading process, respectively. The fields of incremental equivalent plastisc strain added by tensile loading is presented in Figs. 22g and 22h. We observe similar trends as for the 1+6 strands. Again, the fields predicted for the uncompacted strands and the compacted strands without inheritance of compaction induced work hardening are

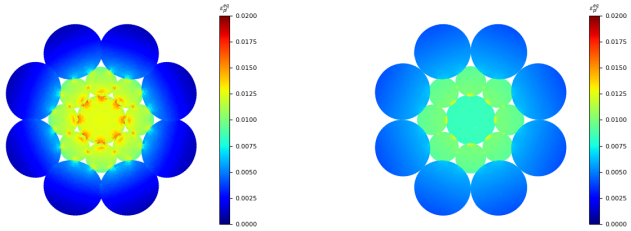

(a) Uncompacted strand, lay length=27.5 mm. (b) Uncompacted strand, lay length=47.5 mm.

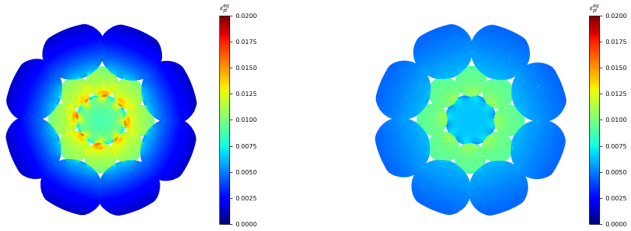

(c) Compacted strand without inherited hardening, lay length=27.5 mm. (d) Compacted strand without inherited hardening, lay length=47.5 mm.

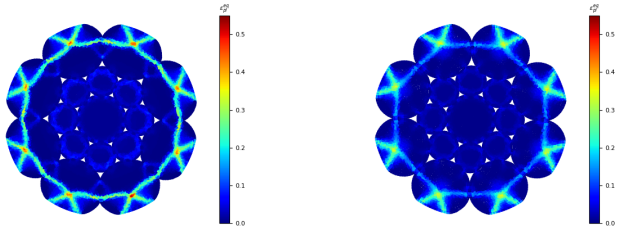

(e) Compacted strand with inherited hardening, lay length=27.5 mm. (f) Compacted strand with inherited hardening, lay length=47.5 mm.

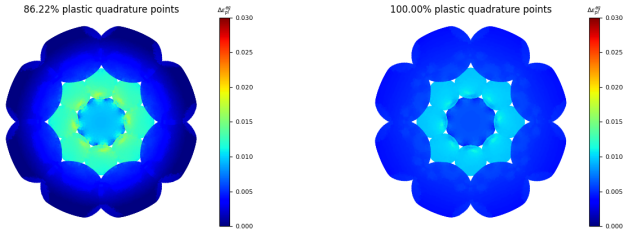

(g) $\Delta\epsilon_{pl}^{eq}$, lay length=27.5 mm. (h) $\Delta\epsilon_{pl}^{eq}$, lay length=47.5 mm.

Figure 22: Strand 17S: Predicted equivalent plastic strains (a.k.a. PEEQ). The bottom two images show the difference of the equivalent plastic strain predicted after compaction and after tensile loading for the case where the equivalent plastic strain in the 3D model is inherited from the 2D compaction model.

different than predicted for the compacted strands with inheritance of compaction induced work hardening.

5 Conclusion

A novel modeling approach to simulate the compaction of strands and the effect of compaction on the strands during subsequent tensile loading is proposed. The approach relies on the consecutive coupling of two elastoplastic finite element models: a 2D plane strain compaction model and a consecutive 3D strand model that uses the geometry and plastic state predicted by the 2D compaction model as initial configuration.

Thanks to the 2D nature of the compaction model, the compaction simulations are fast in contrast to the 3D compaction simulations of [34]. Even though the compaction model is 2D, the effect of the lay length is incorporated thanks to a novel procedure that calculates the ellipticity of the wire cross sections in the strand's cross section. Both finite element models, as well as the coupling of the two, were constructed using commercial finite element software Abaqus, with the help of in-house developed Python scripts and Fortran77 user-subroutines to automate the computational pipeline.

The main results and conclusions based on the results can be listed as follows:

- A good to reasonable match between the experimental and predicted force-strain curves is observed for 3 out of the 4 compacted strands. A less satisfactory match is observed for the 17S strand with the lay length of 27.5 mm (i.e. the most complex strand with the smallest lay length).
- Compaction induced work hardening must be transferred to the 3D model to obtain the same trends of the experimental force-strain curves for different designs.
- The trends of the force-strain curves predicted by the modeling approach are the same as those observed in experiments in terms of a varying lay length and compaction versus no compaction.
- The predicted fields of Von Mises stresses and equivalent plastic strains are completely different when compaction induced geometrical changes and work hardening is incorporated.
- The four aforementioned points are validated for two types of strand designs.

Although the proposed method enables fast compaction simulations and transfers the compaction results to the consecutive simulations of strands during their service life, many aspects relevant for

the mechanics of strands and wire ropes remain to be investigated. For instance, experimental observations show a high degree of preferred grain orientations, implying that anisotropic elastoplasticity may be more suited than the isotropic elastoplasticity that most studies employ. We have also discounted the plastic deformation induced by the manufacturing step in which the wires are twisted together to form the (uncompacted) strand.

Numerous computational enhancements may furthermore improve the accuracy and/or speed of strand and wire rope simulations. Mesh adaptivity tailored to large deformations [7] or fretting fatigue [21] may be one of these approaches. Our future work will however aim to reduce the comutational expenses by decreasing the modeling domain. The starting point for this will be the helical periodic boundary conditions of [15].

6 Acknowledgement

The authors gratefully acknowledge the financial support of the Luxembourg National Research Fund (FNR) for project BRIDGES/2019/MS/14310624/ROPETEST/BEEX. The authors acknowledge the University of Luxembourg supercomputing resources (https://hpc.uni.lu) made available for conducting the research reported in this paper. The authors would like to thank Seong-Hun Song, Thierry Verreet and Christoph Ruffing for the valuable discussions on strands and wire ropes.

A Modeling 2D compaction under quasi-static settings

In this appendix, we show results in case a quasi-static setting is considered instead of the dynamic setting as reported in section 2. Applying a quasi-static solver for the compaction model is only possible if perfect stick is considered, i.e. an infinitely large coefficient of friction, because otherwise the Jacobian is ill-posed. The field of compaction induced work hardening predicted by this quasi-static setting with perfect stick conditions for the 1+6 strand is shown in Fig. 23, together that previously reported in the results section. Fig. 24 shows the different profiles of the compacted strand cross section.

As can be seen, although the spatial pattern of work hardening is similar for both scenarios, the

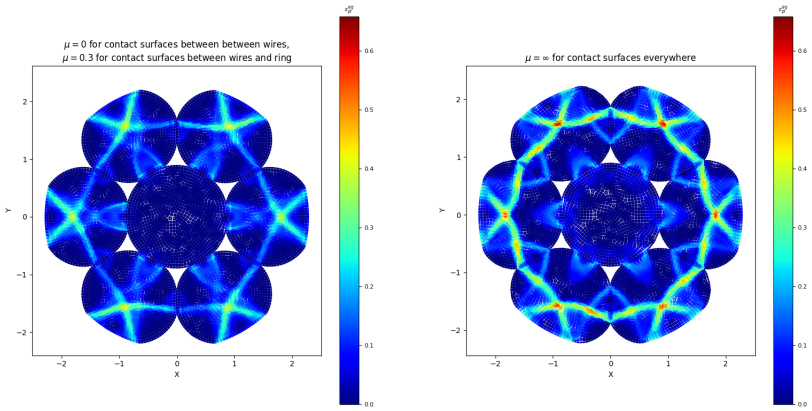

Figure 23: Fields of work hardening after the 2D compaction simulations. Left is under the implicit dynamic setting (Section 2.6) with slippery contact surface (Section 2.5). Right is under the quasi-static setting with rough contact surface. μ denotes the coefficient of friction.

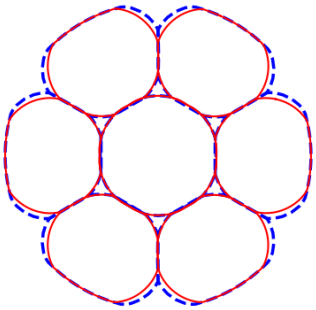

Figure 24: Profiles of compacted strand cross section. The blue dashed lines show the profile predicted under the quasi-static setting with perfect stick conditions. The red solid lines show the profile predicted under the implicit dynamic setting with frictional sliding between the outmost wires and the compaction ring ($\mu = 0.3$) and frictionless sliding between the wires.

magnitudes of the plastic deformation as well as the compacted shapes of the strand cross sections differ noticeably.

References

[1] *On the Design of Wire Rope*, volume 14th Design Automation Conference of *International Design Engineering Technical Conferences and Computers and Information in Engineering Conference*, 09 1988.

[2] CAPSTIAN. What is a steel wire rope? what machine for steel wire rope?, 2020. [Online; accessed March 9, 2021].

[3] Y. J. Chiang. Characterizing simple-stranded wire cables under axial loading. *Finite Elements in Analysis and Design*, 24(2):49–66, 1996.

[4] G. A. Costello. *Theory of Wire Rope*. Springer-Verlag New York, 1997.

[5] V. F. Danenko, L. M. Gurevich, E. Y. Kushkina, and E. B. Gladskikh. New applications of compacted steel strands and wire rope. *Steel in Translation*, 46(11):757–763, Nov 2016.

[6] E. A. de Menezes and R. J. Marczak. Comparative analysis of different approaches for computing axial, torsional and bending stiffnesses of cables and wire ropes. *Engineering Structures*, 241:112487, 2021.

[7] M. Duprez, S. P. A. Bordas, M. Bucki, H. P. Bui, F. Chouly, V. Lleras, C. Lobos, A. Lozinski, P.-Y. Rohan, and S. Tomar. Quantifying discretization errors for soft tissue simulation in computer assisted surgery: A preliminary study. *Applied Mathematical Modelling*, 77:709–723, 2020.

[8] D. Elata, R. Eshkenazy, and M. Weiss. The mechanical behavior of a wire rope with an independent wire rope core. *International Journal of Solids and Structures*, 41(5):1157–1172, 2004.

[9] C. Erdönmez. Computational design of the compacted wire strand model and its behavior under axial elongation. *International Journal of Precision Engineering and Manufacturing*, 20(11):1957–1968, Nov 2019.

[10] C. Erdönmez. Analysis and design of compacted iwrc meshed model under axial strain. *International Journal of Mechanics and Materials in Design*, 16(3):647–661, Sep 2020.

[11] C. Hesch, U. Khristenko, R. Krause, A. Popp, A. Seitz, W. Wall, and B. Wohlmuth. *Frontiers in Mortar Methods for Isogeometric Analysis*, pages 405–447. Springer International Publishing, Cham, 2022.

[12] Q. Hu, F. Chouly, P. Hu, G. Cheng, and S. P. Bordas. Skew-symmetric nitsche's formulation in isogeometric analysis: Dirichlet and symmetry conditions, patch coupling and frictionless contact. *Computer Methods in Applied Mechanics and Engineering*, 341:188–220, 2018.

[13] C. E. Imrak and C. Erdönmez. On the problem of wire rope model generation with axial loading. *Mathematical and Computational Applications*, 15(2):259–268, 2010.

[14] W. Jiang, J. Henshall, and J. Walton. A concise finite element model for three-layered straight wire rope strand. *International Journal of Mechanical Sciences*, 42(1):63–86, 2000.

[15] W. Jiang, M. Yao, and J. Walton. A concise finite element model for simple straight wire rope strand. *International Journal of Mechanical Sciences*, 41(2):143 – 161, 1999.

[16] G. Kosec, J. Slak, M. Depolli, R. Trobec, K. Pereira, S. Tomar, T. Jacquemin, S. P. Bordas, and M. Abdel Wahab. Weak and strong from meshless methods for linear elastic problem under fretting contact conditions. *Tribology International*, 138:392–402, 2019.

[17] K. Kumar, D. Goyal, and S. S. Banwait. Effect of key parameters on fretting behaviour of wire rope: A review. *Archives of Computational Methods in Engineering*, 27(2):549–561, Apr 2020.

[18] A. E. H. Love. *A treatise on the mathematical theory of elasticity*. Cambridge university press, 2013.

[19] M. Magliulo, A. Zilian, and L. A. A. Beex. Contact between shear-deformable beams with elliptical cross sections. *Acta Mechanica*, 231(1):273–291, 2020.

[20] A. Nemov, D. Boso, I. Voynov, A. Borovkov, and B. Schrefler. Generalized stiffness coefficients for iter superconducting cables, direct fe modeling and initial configuration. *Cryogenics*, 50(5):304–313, 2010.

[21] K. Pereira, S. Bordas, S. Tomar, R. Trobec, M. Depolli, G. Kosec, and M. Abdel Wahab. On the convergence of stresses in fretting fatigue. *Materials*, 9(8), 2016.

[22] P. Peterka, J. Krešák, S. Kropuch, G. Fedorko, V. Molnar, and M. Vojtko. Failure analysis of hoisting steel wire rope. *Engineering Failure Analysis*, 45:96–105, 2014.

[23] E. Stanova, G. Fedorko, M. Fabian, and S. Kmet. Computer modelling of wire strands and ropes part i: Theory and computer implementation. *Advances in Engineering Software*, 42(6):305–315, 2011.

[24] E. Stanova, G. Fedorko, M. Fabian, and S. Kmet. Computer modelling of wire strands and ropes part ii: Finite element-based applications. *Advances in Engineering Software*, 42(6):322–331, 2011.

[25] D. Systemes. Abaqus theory manual. *Dessault Systémes, Providence, RI*, 2007.

[26] P. Szade, M. Szot, and B. Kubiś. Thermoelastic effect in compacted steel wire ropes under uniaxial loading. *Quantitative InfraRed Thermography Journal*, 18(4):252–268, 2021.

[27] H. Torgersen. Endurance of compacted steel wire ropes. *Journal of Forest Engineering*, 11(2):43–49, 2000.

[28] M. Torkar and B. Arzenšek. Failure of crane wire rope. *Engineering failure analysis*, 9(2):227–233, 2002.

[29] D. Wang, D. Zhang, S. Wang, and S. Ge. Finite element analysis of hoisting rope and fretting wear evolution and fatigue life estimation of steel wires. *Engineering Failure Analysis*, 27:173–193, 2013.

[30] X.-Y. Wang, X.-B. Meng, J.-X. Wang, Y.-H. Sun, and K. Gao. Mathematical modeling and geometric analysis for wire rope strands. *Applied Mathematical Modelling*, 39(3):1019–1032, 2015.

[31] Wikipedia contributors. Frenet–serret formulas — Wikipedia, the free encyclopedia, 2022. [Online; accessed 13-May-2022].

[32] C. O. Wokem. *Fatigue prediction for strands and wire ropes in tension and bent over sheave wheel*. PhD thesis, Canada, 2015.

[33] W. Wu and X. Cao. Mechanics model and its equation of wire rope based on elastic thin rod theory. *International Journal of Solids and Structures*, 102-103:21 – 29, 2016.

[34] Y. Zeroukhi, G. Vega, E. N. Juszczak, F. Morganti, and K. Komeza. 3d electro-mechanical modeling of conductor after stranding and compacting process simulation. *International Journal of Applied Electromagnetics and Mechanics*, 45:123–129, 2014. 1-4.